A GLOBAL MODE ANALYSIS OF FLAPPING FLAGS

Andres Goza

Division of Engineering and Applied Science
California Institute of Technology
1200 E California Blvd, Pasadena, CA, 91125
ajgoza@gmail.com

Timothy Colonius

Division of Engineering and Applied Science
California Institute of Technology
1200 E California Blvd, Pasadena, CA, 91125
colonius@caltech.edu

ABSTRACT

We perform a global stability analysis of a flapping flag in the conventional configuration, in which the flag is pinned or clamped at its leading edge, and in the inverted configuration, in which the flag is clamped at its trailing edge. Specifically, we consider fully coupled fluid-structure interaction for two-dimensional flags at low Reynolds numbers. For the conventional configuration, we show that the unstable global modes accurately predict the onset of flapping for a wide range of mass and stiffness ratios. For the inverted configuration, we identify a stable deformed equilibrium state and demonstrate that as the flag becomes less stiff, this equilibrium undergoes a supercritical Hopf bifurcation in which the least damped mode transitions to instability. Previous stability analyses of inverted flags computed the leading mode of the undeformed equilibrium state and found it to be a zero-frequency (non-flapping) mode, which does not reflect the inherent flapping behavior. We show that the leading mode of the deformed equilibrium is associated with a non-zero frequency, and therefore offers a mechanism for flapping. We emphasize that for both configurations the global modes are obtained from the fully-coupled flow-flag system, and therefore reveal both the most dominant flag shapes and the corresponding flow structures that are pivotal to flag flapping behavior.

INTRODUCTION

Global stability analysis has been used to elucidate important instability-driving mechanisms in a variety of fluid flows, including bluff body flows (Noack & Eckelmann, 1994), jet flows (Bagheri *et al.*, 2009), and boundary layers (Ehrenstein & Gallaire, 2005). Extending this analysis to fully-coupled flow-structure interaction problems with deforming bodies presents several challenges, and (to our knowledge) has not been done before. We present here an analysis of the fully-coupled problem of flow past a deformable flag in both the conventional and inverted configurations, as depicted in figure 1.

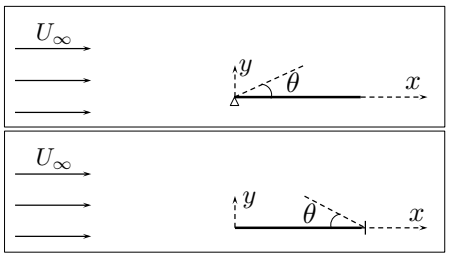

Figure 1: Schematic of the conventional configuration (top) and the inverted configuration (bottom).

Previous stability analyses of conventional and inverted flag flapping considered the governing equations of the flag with the effect of the fluid as a modeled source term using either inviscid (Alben, 2008; Sader *et al.*, 2016) or laminar boundary layer (Connell & Yue, 2007) theory. Thus, the associated modes provide the least damped flag shapes, but do not reveal the corresponding fluid structures that are important to the dynamics. Our present analysis is based on a linearization of the fully-coupled equations of motion, and therefore identifies both important flag shapes and fluid structures.

For thin, elastic flags, the dynamics are governed by the Reynolds number and the dimensionless mass and stiffness ratios (Shelley & Zhang, 2011; Kim *et al.*, 2013), defined as

$$Re = \frac{U_\infty L}{\nu}, M_\rho = \frac{\rho_s h}{\rho_f L}, K_B = \frac{EI}{\rho_f U_\infty^2 L^3} \tag{1}$$

where ρ_s, ρ_f are the solid and fluid densities, respectively; EI is the dimensional bending stiffness of the flag; ν is the kinematic viscosity of the fluid; U_∞ is the freestream flow velocity; and h and L are the thickness and length of the flag, respectively.

Flow past conventional flags has been studied extensively (see Shelley & Zhang (2011) for a review), and we demonstrate here the ability of our global mode analysis to reproduce several results. For example, we compute the flutter boundary at which flapping begins for various parameters and show that it agrees well with the flutter boundary computed by Akcabay & Young (2012) using nonlinear simulations and experiments over Reynolds numbers $O(100-100{,}000)$. We also analyze the global modes for various parameters to identify how important physical mechanisms change across the parameter space.

For inverted flag flapping, there are several possible dynamical regimes that are distinct from conventional flag flapping (Kim *et al.*, 2013; Gurugubelli & Jaiman, 2015). To illustrate this varied behavior, we show in figure 2 a time lapse of the flag position for different regimes. (These figures were created using our nonlinear simulations described below). By decreasing stiffness, the flag can depart its undeformed equilibrium (left plot) and enter small-deflection deformed flapping (second from left plot) (Gurugubelli & Jaiman, 2015). Decreasing stiffness further gives way to large-amplitude flapping (second from right plot), and eventually to large-deflection deformed flapping (right plot) (Kim *et al.*, 2013). We focus here on the small-deflection deformed flapping regime.

Previous stability analyses about the undeformed equilibrium position revealed a bifurcation in which the undeformed equilibrium becomes unstable (Sader *et al.*, 2016; Gurugubelli & Jaiman, 2015). However, the mode associated with this bifurcation is a non-flapping mode (*i.e.*, it contains a zero imaginary part), and it remains an open question to reconcile this modal result with the observed small-deflection deformed flapping behavior. We show here that there is a deformed equilibrium of the inverted flag system, and that a global mode stability analysis about the deflected flag reproduces the correct flapping behavior.

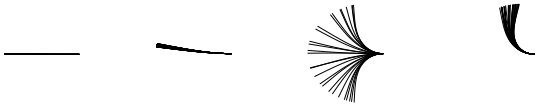

Figure 2: A time lapse of the flag position of an inverted flag in the undeformed equilibrium (left), small-deflection deformed flapping (second from left), large-amplitude flapping (second from right), and large-deflection deformed flapping (right) regimes. The figures were obtained from nonlinear simulations at $Re = 200$, $M_\rho = 0.5$, and stiffnesses (from left to right) of $K_B = 0.5, 0.41, 0.35, 0.13$.

Our analysis is performed in two dimensions (2D) and at relatively low Reynolds numbers ($Re = 500$ for the conventional flag and $Re = 200$ for the inverted flag). Some features of conventional flag flapping were found to be independent of Reynolds number and three-dimensional effects (Akcabay & Young, 2012), and for inverted flags the fact that experiments at $Re = O(10^4)$ (Kim *et al.*, 2013) identified similar dynamical regimes to those seen in 2D simulations at $Re = O(100-1000)$ (Gurugubelli & Jaiman, 2015) suggests some independence from Reynolds number and three-dimensionality. Investigating this issue more completely is an open question that we do not consider here.

NUMERICAL METHOD

Our global mode analysis is based on a linearization of the nonlinear, fully-coupled flow-structure interaction system. These nonlinear equations allow for arbitrarily large flag displacements and rotations, and account for the nonlinear fluid-flag coupling associated with the no-slip boundary condition. We review details about the nonlinear equations and their numerical solution that are salient to the global mode analysis (for more details, see Goza & Colonius (2017)). We then derive the linearized equations and describe the global mode solution approach. Note that the global mode analysis requires a base state that is a steady state solution to the fully coupled equations. We describe these base state computations at the end of this section.

Nonlinear Equations

We treat the fluid with the immersed boundary discrete-streamfunction formulation of Colonius & Taira (2008), and the flag with a geometrically nonlinear Euler-Bernoulli beam formulation. The spatially discrete, temporally continuous equations of the fully-coupled flow-structure system may be written as (see Goza & Colonius (2017) for more details)

$$C^T C\dot{s} = -C^T diag(Ws)Qs + \frac{1}{Re}C^T LCs - C^T E^T(\chi)f \qquad (2)$$

$$M\dot{\zeta} = -R(\chi) + Q(g + W(\chi)f) \qquad (3)$$

$$\dot{\chi} = \zeta \qquad (4)$$

$$0 = E(\chi)Cs - \zeta \qquad (5)$$

Equation (2) represents the Navier-Stokes equations written in a discrete-streamfunction formulation, (3) is the geometrically nonlinear Euler-Bernoulli beam equation, (4) matches the time derivative of the flag position to the flag velocity, and (5) is the interface constraint that the fluid and flag must satisfy the no-slip boundary condition on the flag surface.

In (2)–(5), s, χ, ζ, and f are the discrete streamfunction, flag position, flag velocity, and surface stresses; C and C^T are discrete curl operators that mimic $\nabla\times(\cdot)$; $diag(Ws)Qs$ is a discretization of the advection operator $\mathbf{u}\cdot\nabla\mathbf{u}$ (Colonius & Taira, 2008); L is a discrete Laplacian associated with the viscous diffusion term; $E^T f$ is a "smearing" operator (arising from the immersed boundary treatment) that applies the surface stresses from the flag onto the fluid; M is a mass matrix associated with the flag's inertia; $R(\chi)$ is the internal stress within the flag; Qg is a body force term (*e.g.*, gravity); and QWf is the stress imposed on the flag from the fluid. The fluid equations are spatially discretized using the finite volume scheme of Colonius & Taira (2008), and the structural equations are discretized using a corotational finite element formulation (Criesfield, 1991).

Equation (2) is discretized in time using an Adams Bashforth AB2 scheme for the convective term and a second order Crank-Nicholson scheme for the diffusive term. The flag equations (3)–(4) are discretized using an implicit Newmark scheme. The method is strongly coupled, so the constraint equation (5) is evaluated at the current time step.

A novel feature of our method is the efficient iterative procedure used to treat the nonlinear coupling between the flag and fluid. Many methods use a block-Gauss Seidel iterative procedure, which converges slowly (or not at all) for light structures (Tian *et al.*, 2014). Other methods use a Newton-Raphson scheme, which exhibits fast convergence behavior but requires the solution of linear systems involving large Jacobian matrices (Degroote *et al.*, 2009). Our method employs the latter approach, but we use a block-LU factorization of the Jacobian matrix to restrict all iterations to subsystems whose dimensions scale with the number of discretization points on the flag, rather than on the entire flow domain. Thus, our algorithm inherits the fast convergence behavior of Newton-Raphson methods while substantially reducing the cost of performing an iteration. See Goza & Colonius (2017) for more details.

Linearized Equations And Global Modes

For ease of notation, we define the state vector $y = [s, \zeta, \chi, f]^T$ and let $r(y)$ be the right hand side of (2)–(5). We write the state y as $y = y_b + y_p$, where $y_b = [s_b, \zeta_b, \chi_b, f_b]^T$ is a base state and $y_p = [s_p, \zeta_p, \chi_p, f_p]^T$ is a perturbation. Plugging this expression for y into (2)–(5), Taylor expanding about y_b, and retaining only first order terms in the expansion gives the linearized equations:

$$B\dot{y}_p = Ay_p \qquad (6)$$

where

$$B = \begin{bmatrix} C^T C & & & \\ & M & & \\ & & I & \\ & & & 0 \end{bmatrix}, \qquad (7)$$

$$A = \begin{bmatrix} J^{ss} & 0 & -J^{\chi s} & -C^T E^T \\ 0 & 0 & -K + J^{\chi\chi} & QW \\ 0 & I & 0 & 0 \\ EC & -I & J^{\chi c} & 0 \end{bmatrix}, \qquad (8)$$

$$J^{ss} = -(C^T C)^2 - C^T(diag(Ws_b)Q - diag(Qs_b)W), \qquad (9)$$

and the remaining sub-blocks of the Jacobian matrix A are given in index notation as

$$(J^{\chi s})_{ik} = C^T_{ij} \frac{\partial E^T_{jl}}{\partial \chi_k} (f_b)_l \tag{10}$$

$$(J^{\chi\chi})_{ik} = Q_{ij} \frac{\partial W_{jl}}{\partial \chi_k} (f_b)_l \tag{11}$$

$$(J^{\chi c})_{ik} = \frac{\partial E_{ij}}{\partial \chi_k} C_{jl} (s_b)_l \tag{12}$$

Note that we used $B\dot{y}_b = r(y_b)$ in arriving at the linearized equations (6), and the fact that $diag(Qs)Ws = -diag(Ws)Qs$ in writing (9).

Global modes are eigenvectors v of the generalized eigenvalue problem $Av = \lambda Bv$, where λ is the corresponding eigenvalue. We build and store A and B sparsely and solve the generalized eigenvalue problem using an implicitly restarted Arnoldi algorithm (see Lehoucq *et al.* (1998) for more details).

Base State Computations

Steady state solutions to the fully-coupled equations satisfy (2)-(5) with all time derivate terms set to zero. This may be written as $0 = r(y)$, where $y = [s, \zeta, \chi, f]^T$ is the state vector and $r(y)$ is the right hand side of (2)-(5). This is a nonlinear algebraic system of equations that we solve using a Newton-Raphson method. With this method, the k^{th} guess for the base state, $y^{(k)}$, is updated as $y^{(k+1)} = y^{(k)} + \Delta y$, where

$$\Delta y = -(A(y^{(k)}))^{-1} r(y^{(k)}) \tag{13}$$

Note that the Jacobian matrix A in (13) is the same matrix as in (8) evaluated at $y = y^{(k)}$.

The guess for the state y is updated until the residual at the current guess is less than a desired threshold (*i.e.*, until $r(y^{(k)}) < \varepsilon$). In the results shown below we choose $\varepsilon = 1 \times 10^{-8}$. Our experience is that this approach to computing the base state is robust – often, fewer than six iterations were required to converge to the desired tolerance, even using a poor initial guess of $y^{(0)} = 0$.

Simulation Grid And Mode Normalization

The flow equations are solved using a multidomain approach: the finest grid surrounds the body and grids of increasing coarseness are used as distance from the body increases (see reference [11] for details). For all cases, the immersed boundary spacing is set to be twice that of the flow grid spacing on the finest sub-domain. The domain size of the finest sub-domain was $[-0.2, 1.8] \times [-0.6, 0.6]$ and the total domain size was $[-31.04, 32.04] \times [-19.04, 19.04]$. The grid spacing on the finest domain was $h = 2/400 \approx 0.005$. A grid convergence study was performed on the conventional flag case for $M_\rho = 0.1, K_B = 0.00069$ – decreasing the grid spacing by 30% and increasing the total domain size to $[-40.1, 41.1] \times [-27.08, 27.08]$ caused a change in leading eigenvalue of less than 2%.

Global modes are unique to within a constant scalar multiple. In all cases the modes are scaled such that the norm of the state is unity, $||y||_2 = 1$.

CONVENTIONAL FLAG FLAPPING

We use known results of conventional flag flapping to demonstrate the ability of the global mode analysis to predict the onset of flapping. This comparison with the literature serves the dual purpose of validating our implementation of the analysis. We also investigate the structure of the global modes at different points on the flutter boundary to identify how instability-driving mechanisms change across a range of physical parameters.

Flapping Stability Boundary

The left plot in figure 3 shows the flutter boundary that denotes the onset of flapping for a range of mass ratios and stiffness ratios. The figure includes two lines corresponding to low and high mass ratio fits to empirical data. These fits were computed by Akcabay & Young (2012) from numerical simulations and experiments with Reynolds numbers ranging from $O(100 - 100,000)$. The favorable agreement with these fits attests to the ability of global mode stability analysis to predict the flutter boundary for conventional flags.

The right plot of figure 3 shows the frequencies (given by the imaginary part of the eigenvalue) corresponding to the flutter boundary pictured in the left plot. The black line on the plot is the empirical fit made by Akcabay & Young (2012) to the aforementioned set of experimental and numerical data, and the dashed line is the relation $\sqrt{K_B/M_\rho}$, which is the scaling for the natural flapping frequency of a flag in a vacuum.

At low mass ratios, the fluid inertia plays a substantial role in the flapping dynamics, and the stiffness at which flapping initiates is sensitive to flag mass. In this low-mass regime, the fit of Akcabay & Young (2012) nearly satisfies $M_\rho \approx K_B$, which shows that flutter occurs when the flag inertia is in balance with the internal stresses in the flag. Because of the influence of the fluid, the frequency response is substantially different from the vacuum scaling. At higher masses the fluid inertia becomes less important and the critical stiffness at which flapping initiates is roughly constant. Moreover, because of the weaker influence of fluid inertia, the flapping frequency recovers the vacuum frequency scaling.

Mode Characteristics For Different Parameters

We show in figures 4–6 the leading global modes on the flutter boundary for $M_\rho = 0.05$ ($K_B = 0.005$), $M_\rho = 1$ ($K_B = 0.042$), and $M_\rho = 50$ ($K_B = 0.06$). Note that we change stiffness for the various masses to remain on the flutter boundary, which allows us to identify the modal structure associated with the transition to flapping. In each figure, the real and imaginary part of the modal vorticity is shown on the left and the real and imaginary part of the modal flag shape is shown on the right.

The flag shape has a higher spatial frequency for the low mass ($M_\rho = 0.05$) case than for the other cases (Akcabay & Young, 2012). Note that this is reflected in the modal vorticity, as there are more vortical structures on the flag compared with the higher mass modes. In addition, the higher temporal (flapping) frequency of this low mass flag (as given in the right plot of figure 3) is reflected in the wake structure – there are more vortical structures in the wake, and each structure is compressed compared to the heavier flag modes. When the flag and fluid inertias are in balance ($M_\rho = 1$), "lower mode" flapping occurs, with the spatial frequency of the flag decreased from in the light flag case (Akcabay & Young, 2012). This is matched by fewer vortical structures on the flag. In addition, the lower temporal flapping frequency is marked by an elongation of vortical structures in the flag wake. In the heaviest case, "lower mode" flapping persists with a similar vortical structure on the flag to what was seen in the $M_\rho = 1$ figure. However, the substantially reduced flapping frequency causes a corresponding lengthening of the wake structures.

INVERTED FLAG FLAPPING

Deformed Equilibria And The Initiation of Small-Deflection Deformed Flapping

Recent studies showed that the undeformed equilibrium becomes unstable with decreasing stiffness (Sader *et al.*, 2016; Gurugubelli & Jaiman, 2015). A stability analysis about this equilibrium identifies a zero frequency (non-flapping) unstable mode (Sader *et al.*, 2016; Gurugubelli & Jaiman, 2015), and does not explain the observed small-deflection deformed flapping.

We observe here the existence of a deformed equilibrium state (see figure 7 for equilibria of the inverted flag system for various stiffnesses). A global stability analysis of this deformed equilibrium is associated with purely stable eigenmodes for sufficiently stiff flags. As stiffness is decreased, the least damped mode becomes unstable, and we show in table 1 that this critical stiffness value (and the associated flapping frequency) matches that obtained from the nonlinear simulations. The bifurcation from the stable deformed equilibrium state to small amplitude flapping is a supercritical Hopf bifurcation since it is associated with the transition to instability of a complex eigenvector.

	$K_{B,crit}$	Frequency
nonlinear simulations	0.41 ($\pm$0.01)	0.108
global mode analysis	0.41 ($\pm$0.01)	0.110

Table 1: Critical stiffness ($K_{B,crit}$) at which small-deflection deformed flapping is initiated and the associated flapping frequency. Results are for $M_\rho = 0.05$ (similar results would be obtained for other mass ratios).

To give some intuition for the physical nature of the global modes near the onset of small-deflection deformed flapping, we show in figure 8 the vorticity of the leading mode for $M_\rho = 0.05$ and $M_\rho = 0.5$. As with the conventional flag case, note that increasing mass corresponds to a lengthening in the vortical wake structures to accommodate a decrease in flapping frequencies.

To our knowledge, the deformed equilibria of the flow-inverted flag system have not been reported before, and for completion we discuss them briefly here. For a given stiffness, the deformed equilibrium of the system reflects a balance between internal stresses in the flag and the oncoming fluid forces. Since the equilibrium reflects a static force balance, flag inertia does not play a role and the equilibria depend only on flag stiffness. Note from figure 7 that as the flag stiffness is decreased, the deformed equilibrium is associated with larger flag deflections and wake structures. In figure 7, the deformed equilibrium shown in the middle plot is stable and the system therefore remains in this state for all time. The deformed equilibrium in the right plot is unstable – in nonlinear simulations this unstable equilibrium would give way to large amplitude flapping and complicated vortex shedding behavior. Despite this, the equilibrium may be computed using the techniques described in the Numerical Methods section.

CONCLUSIONS

We presented a global mode stability analysis of the fully-coupled flow structure interaction problem of flow past a deformable flag in the conventional and inverted configuration. We showed that the global mode analysis accurately predicted the onset of flapping in conventional flags, and used the analysis to demonstrate that the small-deflection deformed flapping regime of inverted flags occurs through a supercritical Hopf bifurcation of a deformed equilibrium of the system.

ACKNOWLEDGMENTS

This research was partially supported by a grant from the Jet Propulsion Laboratory (Grant No. 1492185) and by a grant from the Air Force Office of Scientific Research (AFOSR FA9550-14-1-0328). The first author gratefully acknowledges funding from the National Science Foundation Graduate Research Fellowship Program (Grant No. DGE-1144469). We gratefully acknowledge Professor John Sader for helpful discussions on inverted flags.

REFERENCES

Akcabay, Deniz Tolga & Young, Yin Lu 2012 Hydroelastic response and energy harvesting potential of flexible piezoelectric beams in viscous flow. *Physics of Fluids* **24** (5).

Alben, Silas 2008 The flapping-flag instability as a nonlinear eigenvalue problem. *Physics of Fluids* **20** (10).

Bagheri, Shervin, Schlatter, Philipp, Schmid, Peter J & Henningson, Dan S 2009 Global stability of a jet in crossflow. *Journal of Fluid Mechanics* **624**, 33–44.

Colonius, Tim & Taira, Kunihiko 2008 A fast immersed boundary method using a nullspace approach and multi-domain far-field boundary conditions. *Computer Methods in Applied Mechanics and Engineering* **197** (25), 2131–2146.

Connell, Benjamin SH & Yue, Dick KP 2007 Flapping dynamics of a flag in a uniform stream. *Journal of Fluid Mechanics* **581**, 33–67.

Criesfield, MA 1991 *Non-linear finite element analysis of solids and structures, vol. 1*. Wiley, New York.

Degroote, Joris, Bathe, Klaus-Jürgen & Vierendeels, Jan 2009 Performance of a new partitioned procedure versus a monolithic procedure in fluid–structure interaction. *Computers & Structures* **87** (11), 793–801.

Ehrenstein, Uwe & Gallaire, Francois 2005 On two-dimensional temporal modes in spatially evolving open flows: the flat-plate boundary layer. *Journal of Fluid Mechanics* **536**, 209–218.

Goza, Andres & Colonius, Tim 2017 A strongly-coupled immersed-boundary formulation for thin elastic structures. *Journal of Computational Physics* **336**, 401–411.

Gurugubelli, PS & Jaiman, RK 2015 Self-induced flapping dynamics of a flexible inverted foil in a uniform flow. *Journal of Fluid Mechanics* **781**, 657–694.

Kim, Daegyoum, Cossé, Julia, Cerdeira, Cecilia Huertas & Gharib, Morteza 2013 Flapping dynamics of an inverted flag. *Journal of Fluid Mechanics* **736**.

Lehoucq, Richard B, Sorensen, Danny C & Yang, Chao 1998 *ARPACK users' guide: solution of large-scale eigenvalue problems with implicitly restarted Arnoldi methods*. SIAM.

Noack, Bernd R & Eckelmann, Helmut 1994 A global stability analysis of the steady and periodic cylinder wake. *Journal of Fluid Mechanics* **270**, 297–330.

Sader, John E, Cossé, Julia, Kim, Daegyoum, Fan, Boyu & Gharib, Morteza 2016 Large-amplitude flapping of an inverted flag in a uniform steady flow–a vortex-induced vibration. *Journal of Fluid Mechanics* **793**, 524–555.

Shelley, Michael & Zhang, Jun 2011 Flapping and bending bodies interacting with fluid flows. *Annual Review of Fluid Mechanics* **43** (1), 449–465.

Tian, Fang-Bao, Dai, Hu, Luo, Haoxiang, Doyle, James F & Rousseau, Bernard 2014 Fluid–structure interaction involving large deformations: 3D simulations and applications to biological systems. *Journal of Computational Physics* **258**, 451–469.

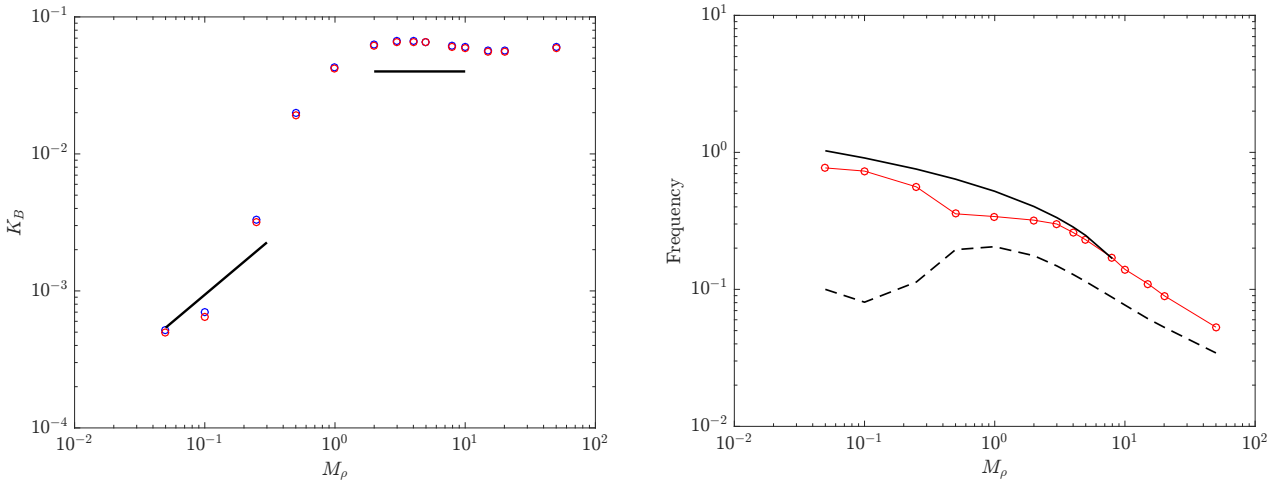

Figure 3: Left: modal prediction of the flutter boundary (○) for various mass (M_ρ) and stiffness (K_B) values (stable modes are in blue and unstable modes are in red), along with empirical fits (——) for small masses ($M_\rho < 1/3$) and large masses ($M > 2$) computed by Akcabay & Young (2012) using a variety of experimental and computational data over Reynolds numbers $O(100-100,000)$. Right: modal frequencies of the unstable mode near the flutter boundary (○-), empirical fit of Akcabay & Young (2012) to the aforementioned numerical and experimental data set (——), and the relation $\sqrt{K_B/M_\rho}$ (- -), which is the frequency scaling for a flag in a vacuum (this scaling must be recovered for sufficiently heavy flags.)

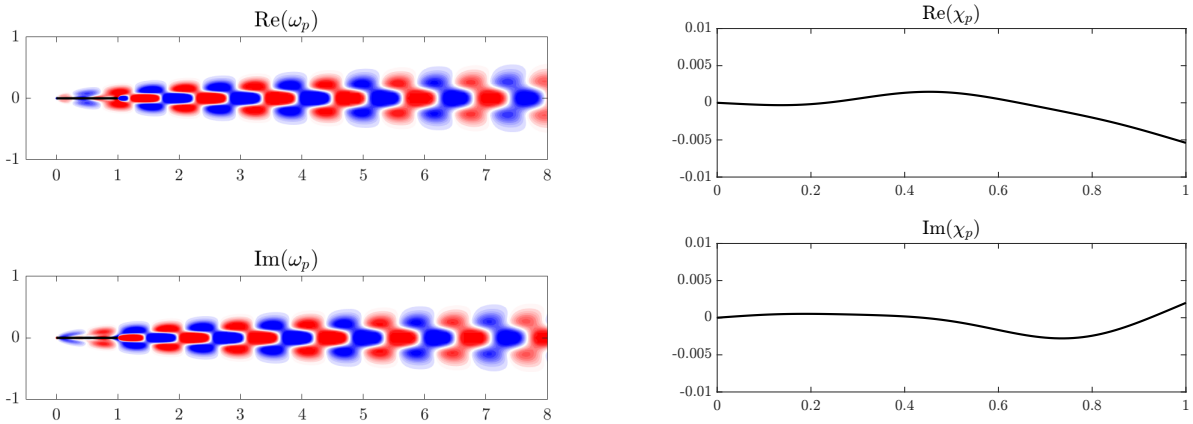

Figure 4: Real and imaginary parts of the modal vorticity (left) and flag shape (right) of a conventional flag for $M_\rho = 0.05$, $K_B = 0.005$ (an unstable mode near the flutter boundary). Contours of vorticity are in twenty evenly spaced increments from -0.2 to 0.2.

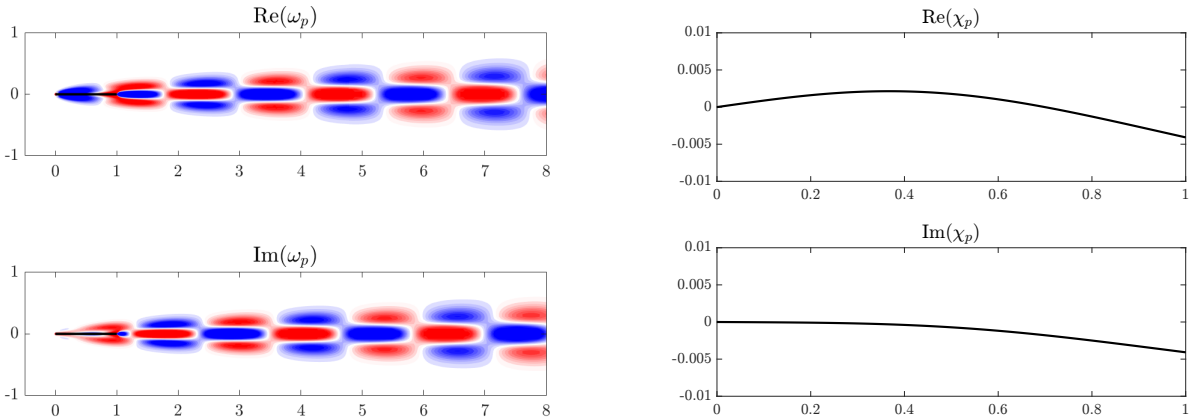

Figure 5: Real and imaginary parts of the modal vorticity (left) and flag shape (right) of a conventional flag for $M_\rho = 1$, $K_B = 0.042$ (an unstable mode near the flutter boundary). Contours of vorticity are in twenty evenly spaced increments from -0.2 to 0.2.

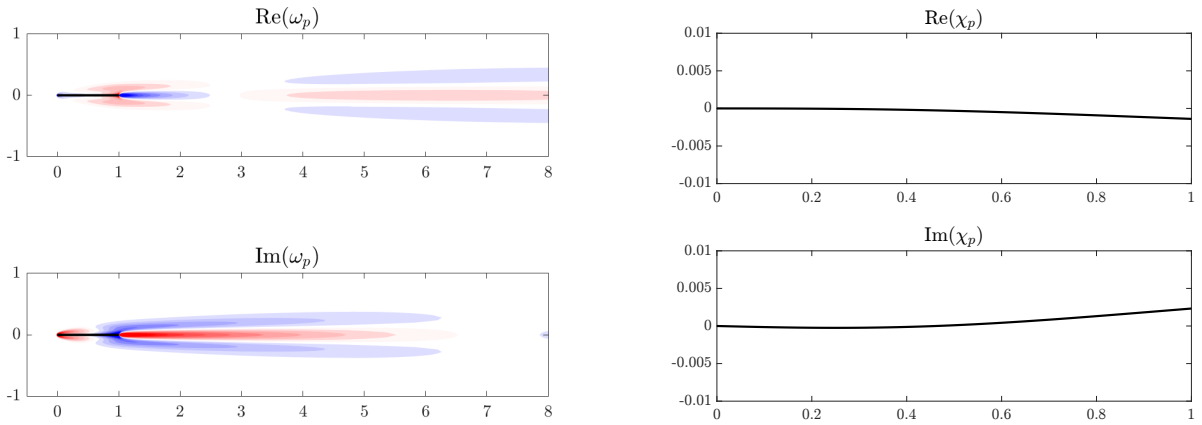

Figure 6: Real and imaginary parts of the modal vorticity (left) and flag shape (right) of a conventional flag for $M_\rho = 50$, $K_B = 0.06$ (an unstable mode near the flutter boundary). Contours of vorticity are in twenty evenly spaced increments from -0.2 to 0.2.

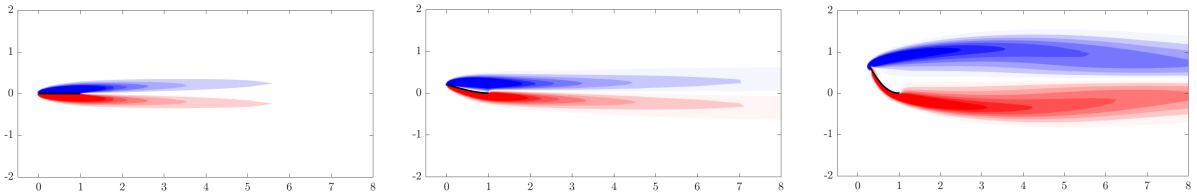

Figure 7: Equilibria of the flow-inverted flag system for $K_B = 0.5$ (left), $K_B = 0.42$ (middle), $K_B = 0.2$ (right). Contours are in 15 evenly spaced increments from -3 to 3.

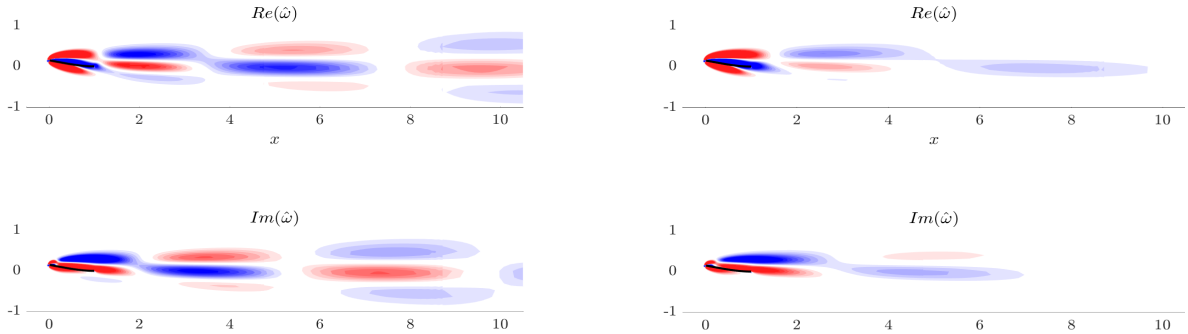

Figure 8: Real and imaginary parts of the modal vorticity of an inverted flag for $K_B = 0.41$ and $M_\rho = 0.5$ (left) and $M_\rho = 5$ (right). Contours of vorticity are in twenty evenly spaced increments from -0.2 to 0.2.